



Fe-Mn oxycarbide anchored on N-doped carbon for enhanced Fenton-like catalysis: Importance of high-valent metal-oxo species and singlet oxygen

Yangzhuo He^{a,b}, Hong Qin^{a,b}, Ziwei Wang^{a,b}, Han Wang^c, Yuan Zhu^{a,b}, Chengyun Zhou^{a,b}, Ying Zeng^{a,b}, Yicheng Li^{a,b}, Piao Xu^{a,b,*}, Guangming Zeng^{a,b,*}

^a College of Environmental Science and Engineering, Hunan University, Changsha 410082, PR China

^b Key Laboratory of Environmental Biology and Pollution Control, Ministry of Education, Hunan University, Changsha 410082, PR China

^c School of Metallurgy and Environment, Central South University, Changsha, Hunan 410083, China



ARTICLE INFO

Keywords:

Peroxymonosulfate activation
Bimetal catalyst
Singlet oxygen
High-valent metal
Wastewater treatment

ABSTRACT

A nonradical oxidation-based peroxyomonosulfate (PMS) activation is an attractive process for pollutant elimination. Herein, a dual-metal-organic framework (MOF) assisted strategy to construct magnetic Fe-Mn oxycarbide anchored on N-doped carbon (FeMn@NC) was proposed for PMS activation. It was found that FeMn@NC-800 displayed superior activity than other comparable counterparts, with nearly 100 % degradation of sulfamethazine (SMZ) within 30 min. Electron paramagnetic resonance and quenching tests revealed that nonradical oxidation ($^1\text{O}_2$ and high-valent metal-oxo species) dominated the SMZ degradation process. Experimental and theoretical calculations demonstrated that FeMn oxycarbide preferred adsorbing the terminal O of PMS, which could improve the PMS oxidation to produce $\text{SO}_5^{\bullet-}$, further generating $^1\text{O}_2$. Moreover, dual active sites could lower the energy barrier to cleave the O–O bond of PMS to form high-valent FeMn = O species. The present study provided a clue to rationally design high-performance heterogeneous catalysts and proposed a novel nonradical-based catalytic oxidation for environmental cleaning.

1. Introduction

Worldwide water pollution caused by naturally emerging organic contaminants and contrived synthetic chemicals has triggered a severe freshwater crisis [1]. In recent decades, heterogeneous peroxyomonosulfate (PMS)-based advanced oxidation processes (AOPs) offer an appealing option for wastewater treatment [2–4]. PMS is one of the most intensively utilized oxidants for generating various reactive oxygen species (ROS) such as sulfate radicals ($\text{SO}_4^{\bullet-}$), hydroxyl radicals ($\bullet\text{OH}$) and singlet oxygen ($^1\text{O}_2$) by UV, ultrasonic, heat, electrochemistry, and transition-metal-based catalysts. The efficiency of PMS-based oxidation system mainly leans on the strong oxidation potential of free radicals (such as $E^0 = 2.5\text{--}3.1\text{ V}$ vs normal hydrogen electrode (NHE) for $\text{SO}_4^{\bullet-}$ and $E^0 = 1.8\text{--}2.7\text{ V}$ vs NHE for $\bullet\text{OH}$) toward emerging organic pollutants [5,6]. However, the high reactivity of these radicals for both target contaminants and competed organics/inorganics lead to the poor catalytic durability, which becomes one of the major obstacles [7,8]. Alternately, nonradical oxidative species (e.g., $^1\text{O}_2$ and high-valent metal) exhibit marked superiority in half-life time, oxidant utilization

efficiency, and selective oxidation of organics [9–11]. Much parallel work has confirmed that the $^1\text{O}_2$ -dominated pathway presents good resistance to common water matrix, and high-valent metal species generated from metal-containing catalysts possess strong oxidizing capacity, which can oxidize organics directly with minimal scavenging [12–17]. At present, the challenge and opportunity in fabrication of a novel heterogeneous catalyst to trigger the nonradical pathway still coexist.

Transition metal catalysts especially those with dual metal sites have been developed as promising catalysts to boost the PMS activation and simultaneously modulate the reaction pathway [18–20]. Recent researches indicated that the energy barrier of O–O bond cleaving of PMS could be effectively reduced through the interaction actions between the two adjacent metals. Besides, the synergistic effect of bimetallic species benefit to facilitate the conversion of $\text{M}^{(n+m)+}$ to M^{n+} (M = metal species), which is considered as a rate-limiting step in Fenton-like reaction [21–23]. On the other hand, transition metal catalysts with dual active sites have realized reactive nonradical pathway on the catalytic site and selective production of $^1\text{O}_2$ and/or high-valent metal toward target

* Corresponding authors at: College of Environmental Science and Engineering, Hunan University, Changsha 410082, PR China.

E-mail addresses: piaoxu@hnu.edu.cn (P. Xu), zgming@hnu.edu.cn (G. Zeng).

pollutant degradation [24,25]. However, the bottleneck and challenge in such sought-after area still exist. First of all, the continuous generation of high-valent metal–oxo species from metal ion is difficult, since the high energy barrier of O–O bond of PMS [26–28]. Additionally, selective production of $^1\text{O}_2$ is also an urgent need due to the production of numerous free radicals such as $\text{SO}_4^{\bullet-}$ and $\bullet\text{OH}$. Besides, the problem of metal aggregation and ions leaching makes the pure metal catalysts less attractive in practical applications. In this regard, seeking an ideal transition metal/carbon precursor and facile method to simultaneously realize the low activation barrier, rapid conversion of metal species and efficient generation of $^1\text{O}_2$ is an important task.

Recently, metal-organic frameworks (MOFs) are popular as precursors for preparation of N-doped carbon-encapsulated transition metal catalysts (NCTMCs), especially Prussian blue analogues (PBAs) with open framework structure, mixed oxidation state and adjustable metal active sites [29–32]. The intrinsic character in composition endows PBAs with good compatibility to fabricate various bimetallic materials with strong redox activity [33]. Considering the inevitable agglomerate of pure PBA-derived metal-based catalysts resulted from their quick crystallization rate, construction of hetero-structured MOFs has drawn intensive interest, which makes dual-MOF hybrid not only possess the combined advantages but also emergent properties [34]. For example, Ganesan et al. reported Co-zeolitic imidazolate framework (ZIF)/Co-Fe-PBA-derived $\text{CoP}_2/\text{Fe}-\text{CoP}_2$ electrocatalysts for the oxygen evolution reaction, in which the Co-ZIF both served as Co metal source and support scaffolds [35]. Ma et al. reported ZIF-67/ZIF-8 @polydopamine-derived Co, N atoms co-doped graphitized carbon for nearly 100 % activation efficiency of PMS to degrade tetracycline [36]. However, such non-radical PMS activation process ($^1\text{O}_2$ and high-valent metal species) based on MOF-derived NCTMCs has rarely been investigated.

Inspired by these, we exploited a dual-MOFs (ZIF-8 and Fe-Mn PBA) assisted approach to construct environmentally friendly Fe-Mn oxy-carbide embedded within N-doped carbon composite as an efficient PMS activator for water remediation. Theoretically, Mn with an atomic radius similar to Fe, have high driving force to bond with Fe, thus forming stable nanoparticles [37]. The combination of Fe with Mn benefits the formation of magnetism, which makes the recycling a time-/energy-saving process. Also, the N-doped carbon layer could protect the enfolded metal core from outside harsh environment without influencing the transport of reactants and products. The sulfamethazine (SMZ, a common antibiotic in water) was selected as a model pollutant due to its serious harm to living being [38]. Herein, the aims of this work were to (i) systematically evaluate the catalytic activity of Fe-Mn based NCTMCs in Fenton-like reaction; (ii) illustrate the formation and crucial role of $^1\text{O}_2$ and high-valent bimetallic $\text{FeMn}=\text{O}$ species by experimental studies and density functional theory (DFT) calculations; (iii) assess the practical applicability of the Fe-Mn based NCTMCs in different pH conditions, organic pollutants, and water matrix. This study is expected to enhance our knowledge toward the nonradical degradation pathway with magnetic NCTMCs in Fenton-like catalysis, which will help to effectively remediate the actual contaminated water.

2. Materials and methods

2.1. Reagents and methods

Information related to the chemicals and materials is provided in Text S1. Characterization (Text S2), analytical methods (Text S3), calculation formula (Text S4), and DFT calculations (Text S5) are summarized in [supporting information](#) as well.

2.2. Catalysts synthesis

2.2.1. Synthesis of cubic ZIF-8 crystals

The ZIF-8 nanocubes were prepared based on the previous study with a few modifications. Specifically, 0.2973 g of $\text{Zn}(\text{NO}_3)_2 \cdot 6\text{H}_2\text{O}$ with

5 mg of hexadecyltrimethylammonium bromide (CTAB) were dissolved in 10 mL of deionized water. Then above solution was rapidly injected into 70 mL of aqueous solution containing 4.54 g of 2-methylimidazole (2-MIM). After the solution were stirred for 20 min at room temperature, the white precipitates were collected and washed with ethanol several times and dried at 60 °C overnight.

2.2.2. Synthesis of ZIF-8/FeMn-PBA

The ZIF-8 nanocubes (44 mg) and $\text{MnCl}_2 \cdot 4\text{H}_2\text{O}$ (76.5 mg) were well-dispersed in 30 mL of ethanol (EtOH) by ultrasound to form a mixture A. Meanwhile, $\text{K}_3\text{Fe}(\text{CN})_6$ (100 mg) was dissolved in 10 mL of deionized water to form a transparent solution B. Then, the B solution was rapidly poured into the A mixture with constant stirring for 2 h at room temperature. At last, the brown solids were centrifuged and washed with water and ethanol. After dried overnight at 60 °C, the ZIF-8/FeMn-PBA crystals were obtained. Besides, FeMn-PBA, MOF precursor-Fe, and MOF precursor-Mn were prepared based on the similar synthesis method without adding ZIF-8, Mn source and Fe source, respectively.

2.2.3. Synthesis of FeMn@NCs

The as-prepared ZIF-8/FeMn-PBA was annealed at 500, 650, 800 and 950 °C for 2 h under nitrogen flow, with a ramp rate of 4 °C·min⁻¹, and the obtained black products were labelled as FeMn@NC-500, FeMn@NC-650, FeMn@NC-800 and FeMn@NC-950, respectively. Zn element was evaporated away owing to its low melting point (419.5 °C) and boiling point (907 °C). For comparison, the FeMn/C, Fe@NC-800 and Mn@NC-800 derived from FeMn-PBA, MOF precursor-Fe, and MOF precursor-Mn were obtained following the same protocol of FeMn@NC-800.

2.3. Experimental procedures

PMS activation was conducted in a 100 mL beaker with 50 mL of SMZ solution (20 mg L⁻¹), PMS (0.5 mM) and catalysts (0.2 g/L) that was shaken with a speed of 160 rpm at 25 °C. Before PMS adding, the catalysts with SMZ solution shaken for 60 min to attain the adsorption-desorption equilibrium. The pH of reaction system was maintained at approximately 5.78. At predetermined time intervals, 1 mL aliquots of reaction solution were withdrawn by syringe, filtered through a 0.22 μm Millipore filter, and quenched with 20 μL of sodium sulfite for subsequent analysis. To assess the reusability of the FeMn@NC-800, the catalyst was separated by magnetism and washed with deionized water and ethanol, and then dried at 60 °C overnight for next cycling. All the degradation experiments were performed in distilled water except the actual water experiments. The detection conditions of SMZ and other organic compounds were presented in [Table S1](#).

3. Results and discussion

3.1. Catalyst characterization

The whole synthesis process of FeMn@NCs was illuminated in [Fig. 1a](#). According to the scanning electron microscopy (SEM) image, ZIF-8 crystals synthesized through a surfactant-assisted strategy were uniform cubic morphology ([Fig. S1a](#)). The microscopic shapes of as-prepared ZIF-8/FeMn-PBA and FeMn@NC-800 were recorded by transmission electron microscope (TEM) and high-resolution transmission electron microscopy (HR-TEM). As shown in [Fig. S1b,c](#), the MOF precursors exhibited irregular nanoparticles (NPs) with an average diameter of 50 nm. After high temperature calcination, well-distributed spherical NPs derived from ZIF-8/FeMn-PBA were observed in [Fig. 1b](#). Interestingly, the enlarged images showed the formation of distinct core-shell structure of FeMn@NC-800, in which the uniform Fe-Mn bimetal particles with diameter of 20 nm were the “core” with N-doped carbon as the “shell” layer ([Fig. 1c,d](#)). The HR-TEM images revealed that interplanar spacing of the carbon matrix was about 0.34 nm, which

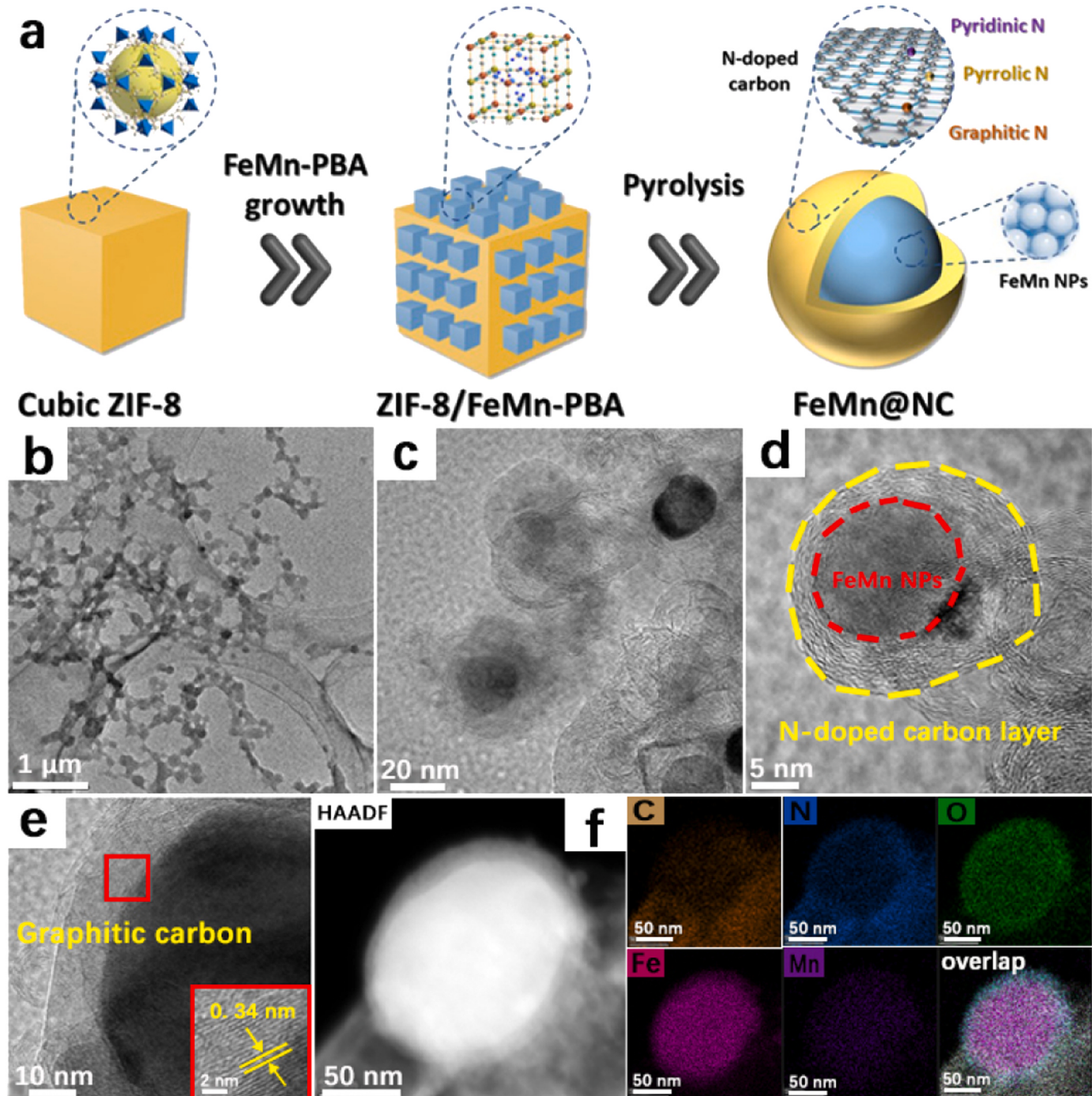


Fig. 1. (a) Schematic illustration of the synthesis process of FeMn@NCs. (b,c) TEM images of FeMn@NC-800. (d,e) HR-TEM images of FeMn@NC-800. (f) HAADF-STEM image and EDS elemental mapping data of FeMn@NC-800.

referred to form of graphite structure in the FeMn@NC-800 nano-architecture (Fig. 1e). TEM element mappings suggested that the carbon surface was overlapped with high contents of N, showing that the graphitic outer shell was doped with ample N. The N-doped carbon could provide numerous active sites for PMS activation to generate more reactive species. Besides, Fe, Mn and O species were evenly distributed over the encapsulated nanoparticles, deducing that the wrapped nanoparticles were more likely composed of Fe, Mn and O element (Fig. 1f). Notably, the core-shell structure could not only prevent the wrapped nanoparticles from aggregation without stemming the mass transport, but also alleviate the metal leaching to avoid the invalidation of catalysts [39–41]. The hybrid structure of N-decorated graphene carbon and

bimetal nanoparticles will fit the bill as an efficient catalyst in PMS-based Fenton-like catalysis.

Fig. S2a displayed X-ray diffractometer (XRD) patterns of FeMn@NCs obtained at different thermal treatment. The main phases of $\text{Fe}_4[(\text{FeCN})_6]_3$ (JCPDS#73-0687) at 17.49, 24.84, 35.42, 39.76, 50.95 and 57.49° in the XRD patterns were observed in FeMn@NC-500. As the temperature increased, the diffraction peaks at 35.04, 40.68, 58.89, 70.40 and 74.04° (marked by yellow) assigned to the $(\text{FeO})_{0.099}(\text{MnO})_{0.901}$ (JCPDS#77-2362) and 43.10, 43.94, 44.74, 45.02, 46.06, 48.66, and 49.32° (marked by blue) identical to $\text{Fe}_{2.7}\text{Mn}_{0.3}\text{C}$ (JCPDS#73-1341) were recorded in FeMn@NC-650, FeMn@NC-800 and FeMn@NC-950. Clearly, the change of peaks

intensity in FeMn@NCs suggested that $(\text{FeO})_{0.099}(\text{MnO})_{0.901}$ phase was dominated when temperature at 650 °C and 800 °C, while it became weaker along with the peaks of $\text{Fe}_{2.7}\text{Mn}_{0.3}\text{C}$ strengthened at 950 °C, indicating the transformation of $(\text{FeO})_{0.099}(\text{MnO})_{0.901}$ to $\text{Fe}_{2.7}\text{Mn}_{0.3}\text{C}$ at higher temperature. As a result, the bimetal NPs in FeMn@NC-800 referred to the complex of iron-manganese oxycarbide. Moreover, two peaks located at 26° and 44° of FeMn@NC-800 and FeMn@NC-950 can be indexed to the (002) and (101) phases in graphite, respectively, demonstrating the formation of graphitic carbon layer when pyrolysis temperature higher than 800 °C.

X-ray photoelectron spectroscopy (XPS) spectra of FeMn@NCs obtained at different temperature were presented in Fig. S2b and Table S2. The XPS wide-scan spectra suggested the presence of C, N, O, Fe and Mn elements in FeMn@NCs. In addition, the intense Zn peak in FeMn@NC-500 demonstrated the incomplete decomposition of MOF precursors at 500 °C. As rising temperature, the content of total N exhibited a downward tendency while the relative metal (Fe + Mn) amounts increased (Fig. S3). Specifically, more metal atoms tended to coordinate with metal itself into nanoparticles, leaving unstable nitrogen species (mainly $\text{C}\equiv\text{N}$) escaped from carbon framework as gas (e.g., CO_2 , NO_x) without coordination. Fe 2p XPS spectra of FeMn@NCs samples were presented in Fig. S4a and Table S3. The binding energy at 708.7 eV of

FeMn@NC-500 corresponded to the Fe species from $[\text{Fe}(\text{CN})_6]^{3-}$. When the temperature climbed to 650 and 800 °C, the $[\text{Fe}(\text{CN})_6]^{3-}$ was decomposed to Oct Fe(II), Oct Fe(III) and Tet Fe(III) at 708.90–713.49 eV in the Fe 2p_{3/2} spectra. As further increasing the temperature, a peak of Fe_3C located at 707.20 eV appeared in FeMn@NC-950, and other two peaks in Fe 2p_{3/2} spectra fell in the range of Fe(III). The XPS Mn 2p spectra of multiple FeMn@NCs catalysts were given in Fig. S4b and Table S4, which can be deconvoluted into three characteristic peaks of Mn(II), Mn(III), and Mn(IV) at around 640.25 eV, 641.20 eV, and 642.40 eV, respectively. Multivalent states of Fe and Mn bimetallic species in FeMn@NCs nanocomposites could trigger redox cycle to facilitate the PMS activation.

In XPS N 1s spectra, three types of pyrrolic N, pyridinic N and graphitic N could be founded in all the FeMn@NCs, and the N-oxides occurred in FeMn@NC-800 and FeMn@NC-950 (Fig. S5a and Table S5). Among them, N-oxides have been proved to be invalid for catalytic activity of carbocatalysts [42]. Specially, the peaks with the binding energy at 397.71 eV in FeMn@NC-500 was well assigned to the N species in $-\text{C}\equiv\text{N}$, and this peak was disappeared with the temperature raised owing to the decomposition of MOF precursors, which agreed with the below TG analysis. Among all the FeMn@NCs samples, FeMn@NC-500 exhibited the highest contents of pyridinic N (8.48 at%) and pyrrolic N

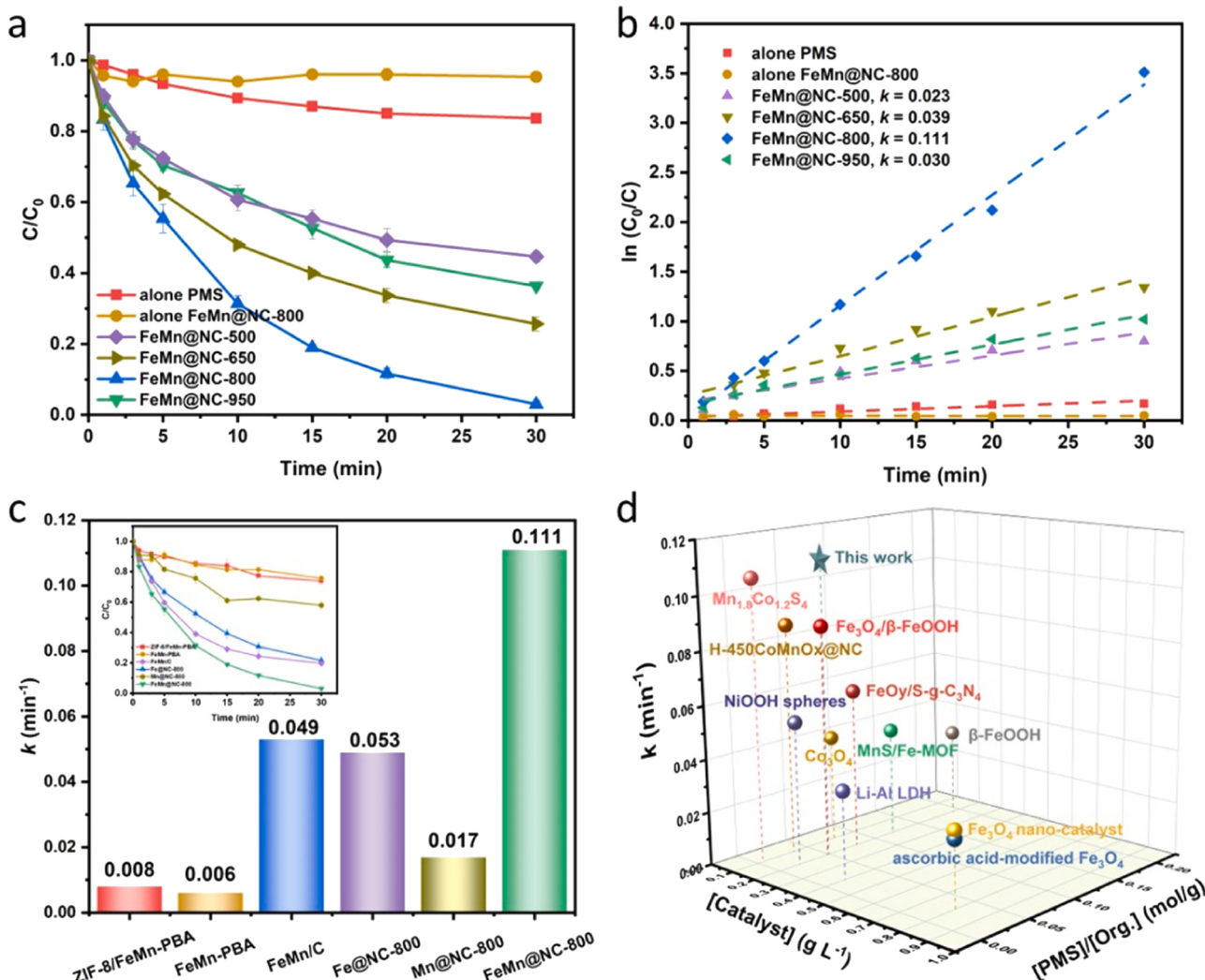


Fig. 2. (a) Effect of calcination temperature on SMZ degradation. (b) Pseudo-first-order kinetic fitting curves of different FeMn@NCs. (c) The calculated first-order rate constants (k) of different catalysts (the inset shows the corresponding degradation curves of SMZ). (d) Comparison of the sulfonamides removal efficiency by FeMn@NC-800 with some reported catalysts. In figure, “Org.” represents organic pollutant. Reaction conditions: $[\text{SMZ}] = 10 \text{ mg L}^{-1}$, $[\text{PMS}] = 0.5 \text{ mM}$, $[\text{catalysts}] = 0.2 \text{ g/L}$, $T = 25^\circ\text{C}$, initial solution $\text{pH} = 5.8$.

(5.84 at%). In contrast, FeMn@NC-800 was endowed with the maximum percentage of graphitic N, which could help to active PMS due to the heightened conductivity and expedited electron transfer. C 1 s spectra (Fig. S5b and Table S6) of different samples can be divided into C–C sp^2 , C–C/C–N sp^3 , C–O, C = O, π – π shake up and C–O 1 s satellite. The peak of C–C sp^2 and π – π shake up satellite can be founded in all samples except FeMn@NC-950, demonstrating the $-\text{C}\equiv\text{N}$ species transformed into graphene carbon below 800 °C and further evolved into gas up to 950 °C, which was corresponded well to the weak graphitic N intensity of FeMn@NC-950 in N 1 s spectra. As for O 1 s spectra, three peaks at 529.56–530.10 eV, 531.24–532.31 eV, and 531.95–533.75 corresponded to metal-O, C = O and C–O (Fig. S5c and Table S7). More detailed characterization of the synthesized catalysts was discussed in Text S6, Fig. S6 and Table S8.

3.2. Catalytic performance evaluation

The activation ability of as-obtained samples to PMS was evaluated by a series of contrast experiments for SMZ decomposition. To exclude the adsorption effect on pollutant removal, adsorption tests within 120 min were carried out and the results showed that all catalysts exhibited low adsorption efficiency (Fig. S7). As shown in Fig. 2a,b,

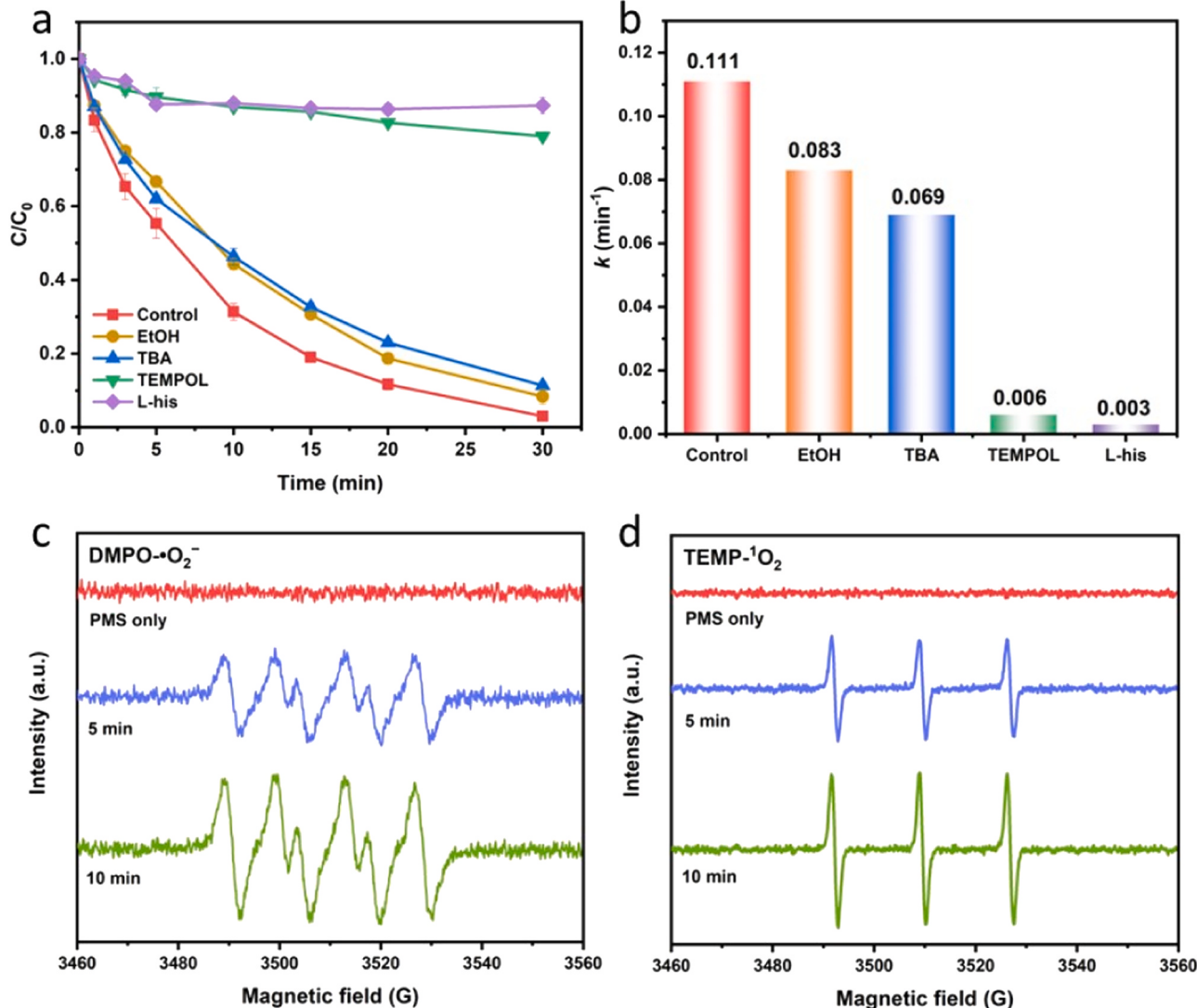


Fig. 3. (a) SMZ degradation curves and (b) the corresponding k value over FeMn@NC-800 catalyst with different quenchers. EPR analysis of (c) DMPO-•O₂⁻, (c) TEMP-¹O₂. Reaction conditions: [SMZ] = 10 mg L⁻¹, [PMS] = 0.5 mM, [catalysts] = 0.2 g/L, T = 25 °C, initial solution pH = 5.8.

catalyst/PMS systems even by several and tens of times under comparable catalyst and PMS dosages (Fig. 2d and Table S9). Furthermore, the influence of operating parameters on SMZ oxidation were conducted and the relative contents were presented in Text S7 and Fig. S8.

3.3. Identification of reactive species

3.3.1. Identification of reactive oxygen species

For the purpose of revealing the ROS occurred during the PMS activation process, quenching experiments and electron paramagnetic resonance (EPR) analysis were implemented (Fig. 3a,b). Armed with α -hydrogen, EtOH is regarded as a scavenger to quench both $\bullet\text{OH}$ and $\text{SO}_4^{\bullet-}$, while tertbutyl alcohol (TBA) without α -H is mainly adopted as a typical trapping agent to $\bullet\text{OH}$. 4-hydroxy-2,2,6,6-tetramethylpiperidinyloxy (TEMPOL) and L-histidine (L-his) exhibit efficient capture capability to $\text{HO}_2\bullet/\bullet\text{O}^{2-}$ and $^1\text{O}_2$, respectively. 5,5-dimethyl-1-pyrroline-N-oxide (DMPO) and 2,2,6,6-tetramethyl-4-piperidinyloxy (TEMP) are generally utilized to capture the $\bullet\text{O}^{2-}$ and $^1\text{O}_2$, respectively. As depicted in Fig. S9a, the SMZ degradation was slightly inhibited in the presence of EtOH at varied levels, implying a spot of $\text{SO}_4^{\bullet-}/\bullet\text{OH}$ in reaction solution. After adding TBA from 25 mM to 500 mM, the SMZ removal efficiency finally diminished to 89 % with the k value of 0.069 min^{-1} (Fig. S9b). Such results manifested the minor role of $\bullet\text{OH}$ in FeMn@NC-800/PMS system. Unusually, more inhibition effect on SMZ oxidation with TBA than with EtOH was witnessed. This can be explained by that TBA was more hydrophobic compared to EtOH, so it was easier to occupy the catalyst surface to hamper the PMS adsorption and activation [43,44]. When increasing TEMPOL concentration from 5 mM to 25 mM, the degradation efficiency was almost the same (Fig. S9c). Only 21 % SMZ was decomposed, which indicated $\text{HO}_2\bullet/\bullet\text{O}^{2-}$ may generated during the degradation process. Besides, strong characteristic peaks corresponding to DMPO- $\bullet\text{O}^{2-}$ adduct were recorded in EPR spectrum, and the increased peak intensity was visualized as the reaction time prolonging to 10 min, further indicating that FeMn@NC-800 could continually activate PMS to produce $\bullet\text{O}^{2-}$ (Fig. 3c). Fig. S9d showed significantly restriction of SMZ degradation even at a low L-his concentration of 5 mM, and such abatement was further improved when the L-his level was raised to 25 mM; relatively, k value dropped sharply to 0.003 min^{-1} , suggesting $^1\text{O}_2$ dominated the oxidative degradation of SMZ. Likewise, three characteristic signals with equal intensities of TEMP- $^1\text{O}_2$ were clearly higher with the reaction proceeding (Fig. 3d). In the FeMn@NC-800/PMS system, the contribution of high-valent metal species and $^1\text{O}_2$ to SMZ degradation were calculated to be 62.2 % and 97.3 %, respectively (the total contribution of the different active species above 100 % may be due to the influence of scavengers).

Further premixing test was conducted to identify the existence of $^1\text{O}_2$ [45]. In detail, if FeMn@NC-800 only acted as an electron mediator between SMZ and PMS, premixing FeMn@NC-800 with PMS will not affect the SMZ degradation. Otherwise, FeMn@NC-800 can consume PMS to generate $^1\text{O}_2$ and thus inhibit SMZ oxidation. As shown in Fig. S10, mixing PMS and catalyst in advance for 5 min and 10 min obviously weaken the catalytic activity, which could be ascribed to the decay of $^1\text{O}_2$ during premixing. Furthermore, the existence of $^1\text{O}_2$ also can be confirmed by replacing the solvent from H_2O to D_2O , since the lifetime of $^1\text{O}_2$ in D_2O (20–32 μs) could be extended more than 10 times than in H_2O (2 μs). As shown in Fig. S11, it was obvious to found that the TEMP- $^1\text{O}_2$ signal became stronger when D_2O was used as solvent, demonstrating the generation of $^1\text{O}_2$ in FeMn@NC-800/PMS system. The valence state change of spent catalysts in XPS spectra implied that Fe(III)/Fe(II) and Mn(IV)/Mn(III)/Mn(II) could provide the electrons to activate PMS for ROS production, and the detailed analysis showed in Text S8, Fig. S12, and Table S10–S13. These results confirmed that radicals combined with non-radicals contributed to the SMZ degradation.

3.3.2. Formation of high-valent metal-oxo species

To demonstrate this assumption that high-valent metal-oxo species probable contained in FeMn@NC-800/PMS system, dimethyl sulfoxide (DMSO), which can be selectively oxidized by high-valent metal through an oxygen-atom-transfer reaction [46], was added into the catalytic reaction. Notably, SMZ removal rate was obviously decelerated with the final k value of 0.042 min^{-1} with the DMSO dosage raising to 20 mM, proving that high-valent metal-oxo species were produced and worked to active PMS (Fig. S13). The degradation decline of SMZ can be attributed to the competition of pollutant molecular and DMSO for high-valent metal-oxo species, which quietly differed from the radical-based degradation pathway. Furthermore, methyl phenyl sulfoxide (PMSO) was reported could be oxidized by Fe(IV), Fe(V) or Mn(V) intermediate to form corresponding sulfone product (methyl phenyl sulfone, PMSO₂) [47,48]. In this regard, PMSO consumption and PMSO₂ generation were utilized to conclusively reveal the contribution of high-valent metal-oxo species. Consistently, an apparent PMSO loss and PMSO₂ production were detected in FeMn@NC-800/PMS system, distinguishing from the system without PMS, which further verified the in-situ formation of high-valent metal intermediates during activation process (Fig. S14). PMS not only decomposed into reactive $^1\text{O}_2$ but also drove the production of high-valent metal-oxo species for pollutant degradation, achieving an overall enhancement of the oxidizing capacity in FeMn@NC-800/PMS system.

It is well-known that many chelating agents (e.g., oxalate and citrate) with specific functional groups could interact with high-valent Fe or Mn to generate the metal-carboxyl complex, leading to the suppression for PMS activation [24]. As shown in Fig. S15a, the obvious impediment of SMZ degradation was recorded when oxalate or citrate was added, suggesting the high-valent metal-oxo species participated in the catalytic reaction. Besides, a weak change of oxalate or citrate concentration was detected, indicating they did not compete with SMZ for reactive species (Fig. S15b). Consistently, the PMS decomposition was also reduced from 50 % to 36 % and 30 % in the presence of oxalate and citrate, respectively (Fig. S15c). Moreover, pyrophosphate, a representative of phosphates ligand, was chosen as a typical chelating reagent to assess the role of Mn(III) in FeMn@NC-800/PMS system [49,50]. Fig. S15a depicted that SMZ degradation was declined after adding pyrophosphate, demonstrating the Mn(III) contributed in the PMS activation. These results verified the existence of high-valent metal-oxo species in the SMZ elimination.

3.4. Catalytic mechanism illustration

3.4.1. Importance of Fe-Mn oxycarbide and origin of $^1\text{O}_2$

Virtually, two pathways involved in $^1\text{O}_2$ production were extensively proposed: (i) PMS acted as electron acceptor. In this process, both metal species and N-decorated carbon can function as the primary active center to supply electrons. After that, the O–O bond of PMS can be cleaved to form large amounts of ROS, which further transformed to $^1\text{O}_2$ ultimately; (ii) PMS served as electron donor, and $^1\text{O}_2$ mainly produced from $\text{SO}_4^{\bullet-}$ self decomposition [51,52]. At this stage, several functional active sites such as C=O, O–C=O, and metal–N_x could provide electrons to deplete the adsorbed PMS for the release of $^1\text{O}_2$ [53]. As a proof of concept, acid treatment with 0.8 M H_2SO_4 solution was applied to remove the Fe and Mn species from FeMn@NC-800 skeleton. After washing 24 h, the residual metal amounts of Fe and Mn decreased from 21.04 % and 27.92–0.92 % and 0.56 %, respectively (detected by Inductively coupled plasma optical emission spectrometer (ICP-OES)). Interestingly, the adsorption capacity of SMZ was dramatically increased to 50 %, while the degradation ability obviously weakened to 34 % (Fig. S16). The acid-washed catalyst basically was pure nitrogen carbon material without metal sites. So, its catalytic activity was originated from different N species, especially graphitic N that has the highest content, which was far from comparable to the metallic catalysts. Such findings demonstrated that the N-doped carbon contributed

little to the organic oxidation, and the PMS activation mainly resulted from the encapsulated bimetal FeMn NPs. FeMn@NC-800 was endowed with the maximum percentage of graphitic N, which could help to active PMS due to the heightened conductivity and expedited electron transfer.

Then, a batch of experiments were implemented to make clear the $^1\text{O}_2$ production path. Firstly, the N_2 purging showed little influence on the SMZ degradation, indicating the $^1\text{O}_2$ was not stemmed from dissolved O_2 (Fig. S17). Owing to very tiny $\bullet\text{OH}$ and $\text{SO}_4^{\bullet-}$ in catalytic system, their transformation to $^1\text{O}_2$ was not considered here. In contrast, the quenching test suggested the stronger inhibition effect on SMZ removal by $\bullet\text{O}_2^{\bullet-}$. For determination, the EPR technique with TEMP in the presence of $\bullet\text{O}_2^{\bullet-}$ quenching agent was performed. Surprisingly, the obvious decrease of the intensities of $^1\text{O}_2$ signals as the activation time prolonging meant that $\bullet\text{O}_2^{\bullet-}$ was the main intermediates for $^1\text{O}_2$ generation (Fig. S18). It was proposed that the recombining rate of $\text{HO}_2\bullet/\bullet\text{O}_2^{\bullet-}$ ($9.7 \times 10^7 \text{ M}^{-1} \text{ s}^{-1}$) is much faster than the reaction rate between $\text{HO}_2\bullet/\bullet\text{O}_2^{\bullet-}$ with electron-rich organics [54]. Besides, 1,3-diphenylisobenzofuran (DPBF) degradation with or without $\text{HO}_2\bullet/\bullet\text{O}_2^{\bullet-}$ scavenger was performed to further verify the evolution path of $^1\text{O}_2$. As shown in Fig. S19, only faint DPBF was degraded when adding TEMPOL; conversely, 33 % degradation efficiency of DPBF was observed in the blank group, illustrating the $\text{HO}_2\bullet/\bullet\text{O}_2^{\bullet-}$ contributed to the formation of $^1\text{O}_2$. As for the second $^1\text{O}_2$ production approach, linear sweep voltammetry (LSV) analysis was conducted to monitor charge migration in different systems. As depicted in Fig. S20, the current density of the FeMn@NC-800 electrode was continuously enhanced after adding PMS and SMZ in sequence, implying electrons transferred from PMS and SMZ to the catalysts, in which PMS decomposed into $\text{SO}_5^{\bullet-}$ as intermediate. Owing to its high reaction rate ($\approx 2 \times 10^8 \text{ M}^{-1} \text{ s}^{-1}$) as well as low activation energy ($7.4 \pm 2.4 \text{ kcal mol}^{-1}$), the produced $\text{SO}_5^{\bullet-}$ rapidly

coupled with each other to generate $\text{S}_2\text{O}_8^{2-}$, SO_4^{2-} , and $^1\text{O}_2$ [55,56]. From above results and analysis, it could be concluded that $^1\text{O}_2$ in FeMn@NC-800/PMS system not only came from ROS transformation but also $\text{SO}_5^{\bullet-}$ self-reaction.

3.4.2. Theoretical verification of high-valent $\text{FeMn} = \text{O}$ and $^1\text{O}_2$ generation

DFT calculations were conducted to reveal the formation of high-valent metal-oxo species and activation mechanisms. The calculated model was simulated using a $(\text{FeO})_{0.099}(\text{MnO})_{0.901}/\text{NC}$ according to XRD analysis (Fig. 4c). Fig. 4a depicted the energy profiles of generated intermediates (INT) during PMS activation to trace the origin of high-valent $\text{FeMn} = \text{O}$. Initially, PMS molecular was adsorbed onto the catalyst surface as $^*\text{HOSO}_4$, followed by chemically bounding to bimetal active sites with terminal peroxy O atom to produce $=\text{FeMn} - \text{O}(\text{H})\text{OSO}_3^-$ complex (INT 1), with a free energy of -1.69 eV . The successful adsorption manifested that both Fe and Mn sites of FeMn@NC-800 have strong affinity for PMS. Then, proton transfer occurred on $=\text{FeMn} - \text{O}(\text{H})\text{OSO}_3^-$ complex, giving rise to the generation of $=\text{FeMn} - \text{OOSO}_3^{2-}$ (INT 2) with a calculated energy difference of 0.93 eV with Initial. Finally, the O–O bond of $=\text{FeMn} - \text{OOSO}_3^{2-}$ was radicalized and dissociated to spontaneously produce high-valent bimetallic $\text{FeMn} = \text{O}$ reactive species, and the energy was only 0.11 eV in this stage. In conclusion, the required total energy for high-valent $\text{FeMn} = \text{O}$ formation was calculated to be 2.62 eV , lower than that for the generation of high-valent $\text{Mn} = \text{O}$ (3.26 eV) and high-valent $\text{Fe} = \text{O}$ (2.82 eV) species (Fig. S21). Thus, the result illustrated that the combination of Fe with Mn could reduce the reaction barrier for energetically favorable production of high-valent bimetal active species.

To uncover the role of FeMn bimetal nanoparticle and N-doped carbon in the generation of ROS, the adsorption energy (E_{ads}) of PMS on

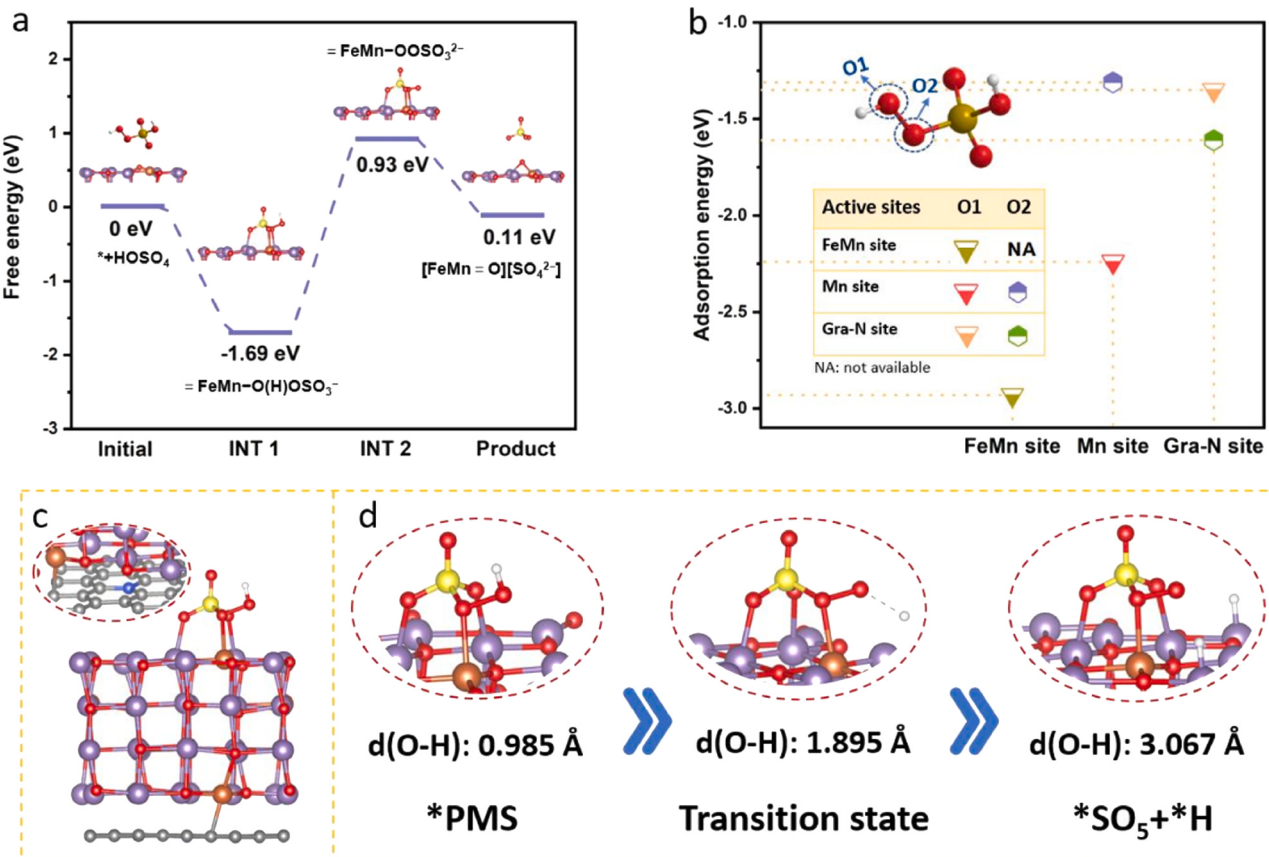


Fig. 4. (a) Energy profiles for the generation of high-valent $\text{FeMn} = \text{O}$ species. (b) DFT calculations of PMS adsorption onto the different sites of catalysts (inset: molecular model of PMS). (c) Optimized configuration of PMS adsorbed on $(\text{FeO})_{0.099}(\text{MnO})_{0.901}/\text{NC}$. The H, C, N, O, S, Mn and Fe atoms are represented by white, grey, blue, red, yellow, purple and orange spheres, respectively. (d) Evolution process of PMS into $\text{SO}_5^{\bullet-}$ on FeMn@NC-800.

different active sites were calculated. As shown in **Fig. 4b**, **Fig. S22** and **Table S14**, the E_{ads} of O2 site in PMS on graphitic N (Gra-N) site of FeMn@NC-800 was -1.61 eV, which promoted the reduction of PMS to produce $\text{SO}_4^{\bullet-}$ and $\bullet\text{OH}$, further generating $\bullet\text{O}_2^-$. Notably, when O2 of PMS adsorbed on FeMn bimetal site, the PMS would decomposition owing to the particularity of the structure. So, this process is not available. In contrast, FeMn bimetal site preferentially adsorbed the O1 site of PMS with the E_{ads} of -2.93 eV, stronger than single metal Mn site with the E_{ads} of -2.24 eV, resulting in the oxidation of PMS on bimetal sites to $\text{SO}_5^{\bullet-}$ by the release of H atom and e^- . **Fig. 4d** and **Fig. S23** displayed the evolution process of PMS into $\text{SO}_5^{\bullet-}$ on FeMn@NC-800. The

bond length of O-H was calculated to be 0.985 Å, 1.895 Å and 3.067 Å in the *PMS, transition state and ${}^*\text{SO}_5 + {}^*\text{H}$, respectively. The prolonged bond length demonstrated the O-H was broken and the H atom was loss from PMS. According to the calculation and analysis above, the active region for ${}^1\text{O}_2$ generation mainly originated from FeMn bimetal species, while the N-doped carbon played the dual function of producing free radical and preventing the metal active center from leach and aggregation, guaranteeing the continuous activation of FeMn@NC-800. In such catalytic system, ${}^1\text{O}_2$ working together with high-valent metal intermediates is expected to expand the toolbox for the nonradical pathway for wastewater decontamination.

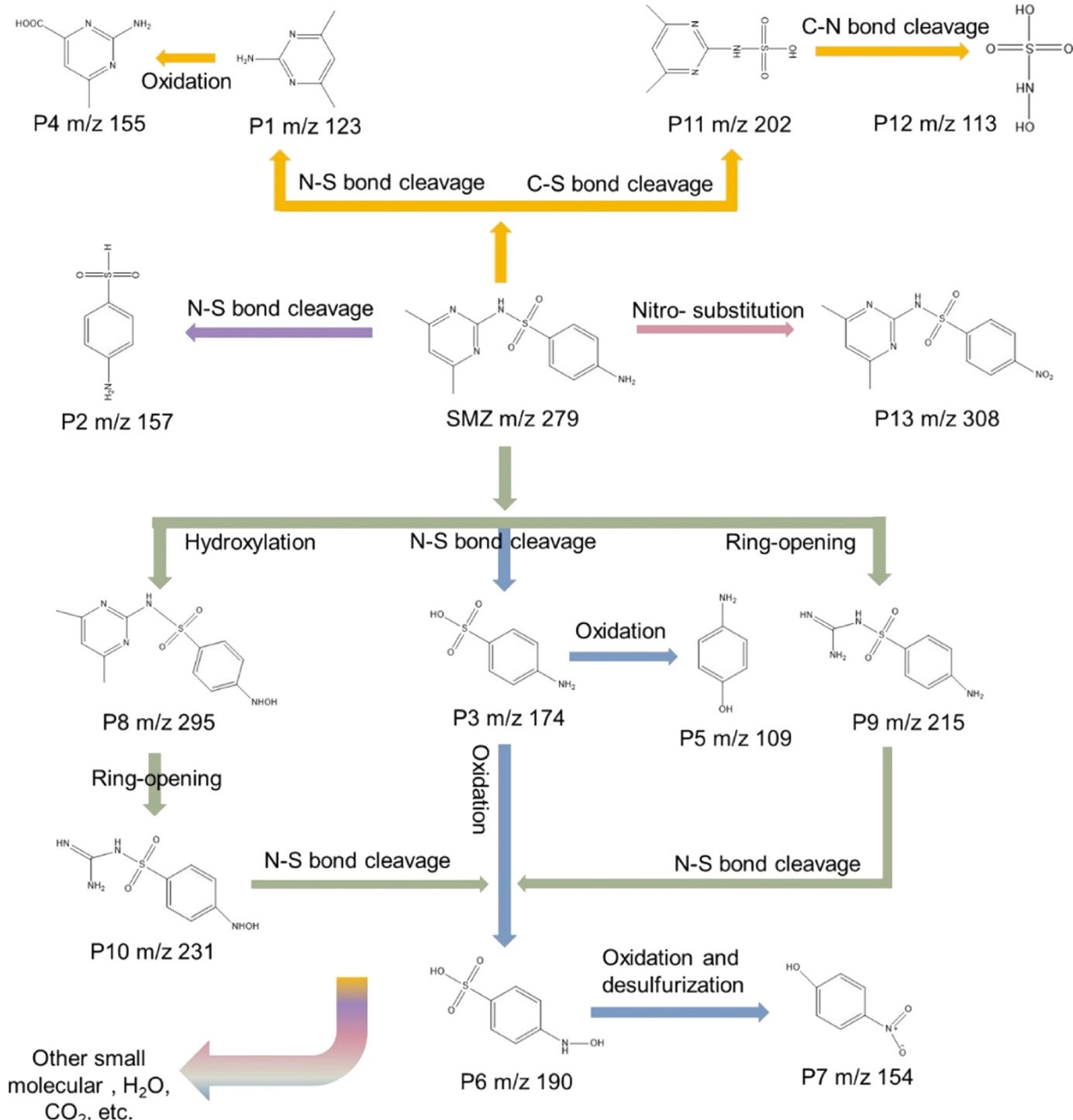


Fig. 5. The proposed degradation pathways of SMZ in the FeMn@NC-800/PMS system.

3.5. Proposed SMZ degradation pathways

The degradation intermediates of SMZ in FeMn@NC-800/PMS system were detected by ultra-high-performance liquid chromatography-mass spectrometry (UPLC-MS) technique. In the whole oxidation process, a total of 13 intermediates were identified, and the obtained mass spectra (MS, MS^2) and their corresponding ion flow curves were shown in Fig. S24-S26. Besides, the predicted structures of 13 intermediates were given in Table S15. Based on the analytic results and previous relevant studies, the possible degradation pathway of SMZ was proposed in Fig. 5 and mainly included N-S/C-S/C-N bond cleavage, nitro- substitution, hydroxylation reaction, ring-opening, oxidation, and desulfurization process.

Specifically, the N-S bond of SMZ molecular was firstly broken to form P1 (m/z 123) with pyrimidine ring, P2 (m/z 157) and P3 (m/z 174) with aniline ring. For the pyrimidine ring substituent, owing to the easy oxidation of methyl group in P1 by ROS produced in FeMn@NC-800/PMS system, P1 was further oxidized to generate P4 (m/z 155). With respect to the aniline ring component, the oxidation rapidly occurred in P3 and thus generated P5 (m/z 109) and P6 (m/z 190). Subsequently, the resulted P6 was converted into P7 (m/z 154) through oxidation and desulfurization reaction, where the N atom of amino group in benzene ring was oxidized into nitro group, accompanied by SO_4^{2-} releasing. On the other hand, the strong negative charge between benzene ring and N atom caused the N-H bond vulnerable to ROS, thus leading to the generation of P8 (m/z 295) by hydroxylation reaction. Then, the pyrimidine rings of SMZ and produced P8 continued to undergo ring-opening reaction to form P9 (m/z 215) and P10 (m/z 231), respectively. After by the N-S bond breaking, the resulted P9 and P10 was decomposed into P6. In addition, the C-S bond of SMZ could be broken to produce P11 (m/z 202) that armed with $-SO_3H$ fragment. Under the attack of ROS, the cleavage of C-N bond in P11 leaded to the generation of P12 (m/z 113). Meanwhile, SMZ molecular could be experienced the

nitro- substitution to form P13 (m/z 308). Finally, these resulted intermediates would continue to converted into H_2O , CO_2 , and other low molecular compounds.

3.6. Reusability test

To assess the stability and reusability of FeMn@NC-800, recycling experiment was carried out. As shown in Fig. 6a, the degradation efficiency of SMZ over spent FeMn@NC-800 still achieved approximately 80 % after four successive cycles. The slight decline in catalytic performance could be resulted from the block active sites by the adsorbed PMS or degradation intermediates. XRD pattern of FeMn@NC-800 before and after activation reaction were almost the same, indicating that the crystal structure of FeMn@NC-800 was indeed stable during the oxidation process (Fig. S27). Very intriguingly, the catalytic property of spent FeMn@NC-800 was almost recovered through heat regeneration at 350 °C after 4 cycles, suggesting that these adsorbed molecules on catalyst surface could be readily removed by annealing processing. The mineralization efficiency of SMZ was also tested and the result showed that approximately 60 % of total organic carbon (TOC) removal was obtained (Fig. 6b). The leaching concentration of Fe and Mn ions in FeMn@NC-800/PMS system was evaluated during reaction process. As presented in Fig. 6c, the amount of dissolved Fe and Mn ions in solution were determined to be lower than 0.1 mg L⁻¹, far less than the limitation of Fe (0.3 mg L⁻¹) and Mn (5 mg L⁻¹) established by the Chinese National Standard (GB 8978-1996). Furthermore, homogeneous reaction with the same content of leached Fe and Mn ions in FeMn@NC-800 was conducted. The result showed that neglectable SMZ removal was observed after 30 min, demonstrating the homogeneous system contributed little to activate PMS for SMZ decomposition. Based on the results above, magnetic FeMn@NC-800 catalyst showed excellent stability and reusability, and its core-shelled structure was effective on the prevention of secondary pollution caused by metal leaching.

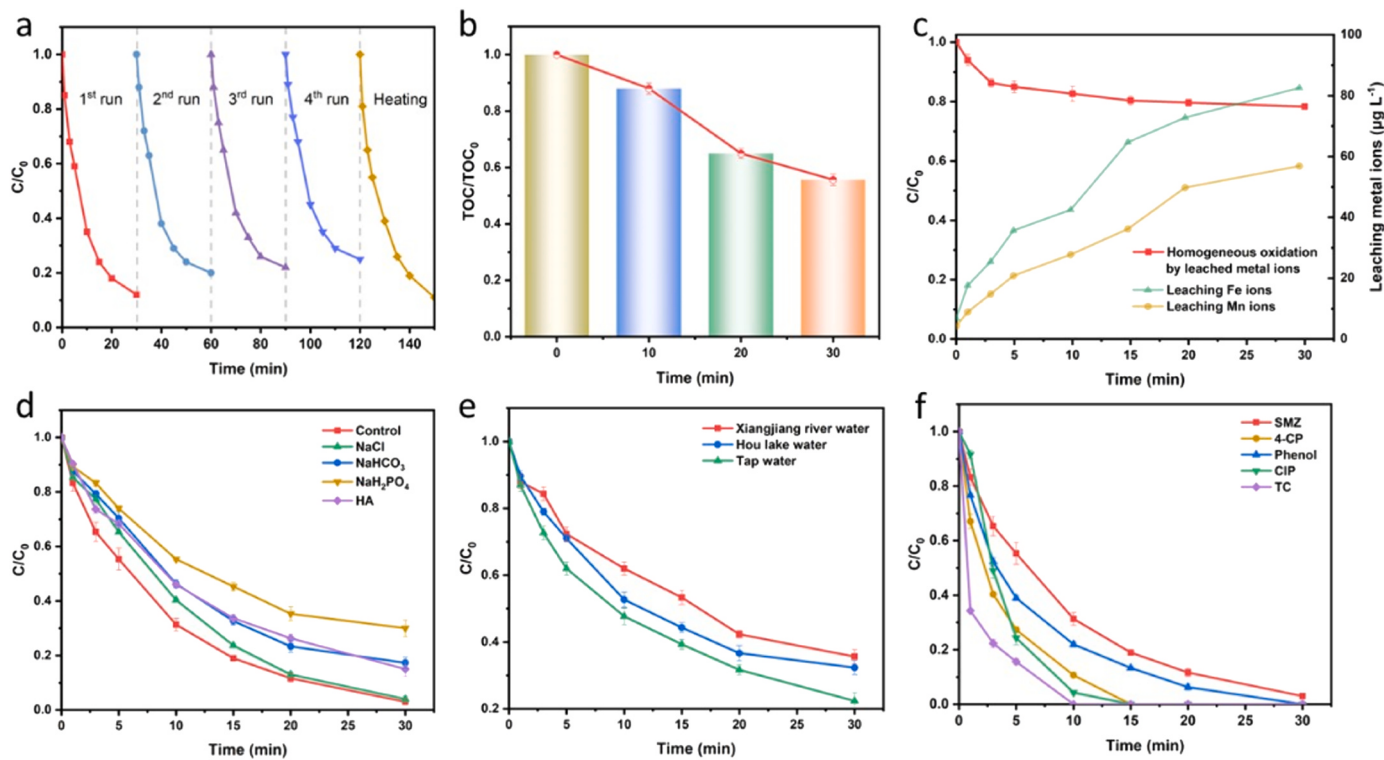


Fig. 6. (a) Recyclability of FeMn@NC-800 for SMZ removal. (b) TOC removal efficiency by FeMn@NC-800. (c) Leaching concentration of Fe and Mn ions and homogeneous oxidation of SMZ by the leaching metal ions. (d) Effect of Cl^- , HCO_3^- , $H_2PO_4^-$, and HA on SMZ degradation in the FeMn@NC-800/PMS system. (e) SMZ degradation in real waters. (f) Degradation of phenol, CIP, TC, SMZ and 4-CP in the FeMn@NC-800/PMS system. Reaction conditions: [SMZ] = 10 mg L⁻¹, [PMS] = 0.5 mM, [catalysts] = 0.2 g/L, T = 25 °C, initial solution pH = 5.8.

3.7. Environmental resistance of FeMn@NC-800 in PMS activation system

In a real water body, the ubiquitous background substances could inevitably interfere with the catalytic efficiency of Fenton-like reaction. To test the feasibility of the FeMn@NC-800 in practical water matrices, natural organic matter such as humic acid (HA) and inorganic anions including Cl^- , HCO_3^- , and H_2PO_4^- were added into the FeMn@NC-800/PMS system. As shown in Fig. 6d and Fig. S28, these background substances caused a certain influence on the Fenton-like process, following the order of $\text{Cl}^- < \text{HA} < \text{HCO}_3^- < \text{H}_2\text{PO}_4^-$. The inconspicuous interference of common natural organic matter and inorganic anions on SMZ degradation could be attributed to several aspects. (i) these common background substances may react directly with ROS generated in catalytic system, thus reducing reactive species levels and forming other less active radicals, such as $\bullet\text{Cl}$, $\bullet\text{Cl}_2$, and ClOH^\bullet from Cl^- , and HCO_3^\bullet and CO_3^\bullet from HCO_3^- [57,58]. (ii) these competed matters presented in water may chelate with multivalent metal ions on catalyst surface and occupy the active sites, thus impeding the interaction between PMS and catalysts [59]. Satisfactorily, the overall efficiency of SMZ oxidation is still favorable at any of tested concentration, suggesting the FeMn@NC-800/PMS system-mediated nonradical degradation pathway had strong resistance to interference from actual water backgrounds.

To furnish further evidence to support the excellent tolerance ability of FeMn@NC-800 in practical environment, the degradation performance of SMZ was tested in actual waters from Xiangjiang River, Hou Lake and tap water (characteristics shown in Table S16). Owing to the integrated effects of inorganic ions, natural organic matters and microflora, a little reduction in oxidation efficiency was recorded in FeMn@NC-800/PMS system, which further revealed the promising potential of FeMn@NC-800 in practical wastewater treatment (Fig. 6e). Furthermore, the universality of as-prepared catalysts to degrade other commonly used organic pollutants was evaluated. Impressively, FeMn@NC-800 exhibited a superior removal efficiency for p-chlorophenol (4-CP), phenol, ciprofloxacin (CIP), and tetracycline (TC) (Fig. 6f). As reported, phenolic compounds enrichment on the catalyst that depends on their hydrophobicity. 4-CP with more hydrophobic property was easier degraded than phenol. Thus, the generated interface ROS by catalyst preferred to attack the enriched 4-CP, leading to the faster removal [44]. Besides, $-\text{S}(\text{O})_2-$ in SMZ and $-\text{F}$ in CIP as strong electron-withdrawing group made a contaminant less active toward ROS attack [60], whereas TC with electron-donating groups such as hydroxyl and amido groups can be oxidized by nonradical reactive species more readily [61–63]. In short, the FeMn@NC-800 combined with PMS system was found to be stable and showed remarkable ability to abate different pollutants in wastewater treatment.

4. Conclusion

A highly efficient and stable NCTMC with magnetism is always desired for Fenton-like catalysis. This work proposed a facile approach via dual MOFs as co-precursors to synthesized magnetic Fe-Mn oxy-carbide anchored on N-doped carbon to activate PMS for wastewater remediation. The FeMn@NC-800 presented superior catalytic activity and stability, far outperforming other as-prepared counterparts. EPR measurements and quenching reactions verified ${}^1\text{O}_2$ and high-valent metal-oxo species as the main reactive species during PMS activation over FeMn@NC-800. Based on DFT calculations, the evolution of ${}^1\text{O}_2$ and high-valent $\text{FeMn}=\text{O}$ were identified. The FeMn bimetal site adsorbed the terminal O of PMS and followed by oxidizing to SO_5^\bullet , further producing ${}^1\text{O}_2$, while N-doped carbon was responsible for the generation of SO_4^{2-} and $\bullet\text{OH}$, further generating $\bullet\text{O}^{2-}$, and finally converting to ${}^1\text{O}_2$. Besides, Fe-Mn dual active sites could reduce the energy barrier of O–O bond cleaving of PMS, making for the production of high-valent $\text{FeMn}=\text{O}$ species. Furthermore, FeMn@NC-800 exhibited outstanding reusability and excellent applicability for remediation of

realistic wastewater. High oxidation capacity for different organic pollutants corroborated the excellent applicability of FeMn@NC-800. This work developed a new vision to the nonradical oxidation of emerging organic pollutants over well-designed NCTMCs in Fenton-like catalysis.

CRediT authorship contribution statement

Yangzhuo He: Methodology, Investigation, Data curation, Visualization, Writing – original draft. **Hong Qin:** Methodology, Investigation, Data curation. **Ziwei Wang:** Methodology, Software, Writing – review & editing. **Han Wang:** Investigation, Formal analysis, Software. **Yuan Zhu:** Resources, Software. **Chengyun Zhou:** Visualization, Resources. **Ying Zeng:** Software, Validation. **Yicheng Li:** Software, Validation. **Piao Xu:** Conceptualization, Supervision, Project administration, Funding acquisition, Writing – review & editing. **Guangming Zeng:** Conceptualization, Supervision, Funding acquisition.

Declaration of Competing Interest

The authors declare that they have no known competing financial interests or personal relationships that could have appeared to influence the work reported in this paper.

Data availability

Data will be made available on request.

Acknowledgements

This work was supported by the National Natural Science Foundation of China (52070077, U20A20323), the National Program for Support of Top-Notch Young Professionals of China (2014), the Program for Changjiang Scholars and Innovative Research Team in University (IRT-13R17), the Hunan Provincial Science and Technology Plan Project (2022JJ20013, 2021JJ40098), and the Science and Technology Innovation Program of Hunan Province (2022RC1121), the Fundamental Research Funds for the Central Universities (531118010226).

Appendix A. Supporting information

Supplementary data associated with this article can be found in the online version at doi:10.1016/j.apcatb.2023.123204.

References

- [1] C. Chu, J. Yang, X. Zhou, D. Huang, H. Qi, S. Weon, J. Li, M. Elimelech, A. Wang, J.-H. Kim, Cobalt single atoms on tetrapyridomacrocyclic support for efficient peroxymonosulfate activation, *Environ. Sci. Technol.* 55 (2021) 1242–1250.
- [2] J. Lee, U. von Gunten, J.-H. Kim, Persulfate-based advanced oxidation: critical assessment of opportunities and roadblocks, *Environ. Sci. Technol.* 54 (2020) 3064–3081.
- [3] J. Miao, J. Song, J. Lang, Y. Zhu, J. Dai, Y. Wei, M. Long, Z. Shao, B. Zhou, P.J. J. Alvarez, L. Zhang, Single-atom MnN₅ catalytic sites enable efficient peroxymonosulfate activation by forming highly reactive Mn(IV)-Oxo species, *Environ. Sci. Technol.* 57 (2023) 4266–4275.
- [4] W. Liu, C. Nie, W. Li, Z. Ao, S. Wang, T. An, Oily sludge derived carbons as peroxymonosulfate activators for removing aqueous organic pollutants: performances and the key role of carbonyl groups in electron-transfer mechanism, *J. Hazard. Mater.* 414 (2021), 125552.
- [5] S.-S. Lin, M.D. Gurol, Catalytic decomposition of hydrogen peroxide on iron oxide: kinetics, mechanism, and implications, *Environ. Sci. Technol.* 32 (1998) 1417–1423.
- [6] P. Shao, J. Tian, F. Yang, X. Duan, S. Gao, W. Shi, X. Luo, F. Cui, S. Luo, S. Wang, Identification and regulation of active sites on nanodiamonds: establishing a highly efficient catalytic system for oxidation of organic contaminants, *Adv. Funct. Mater.* 28 (2018) 1705295.
- [7] S. Waclawek, H.V. Lutze, K. Grubel, V.V.T. Padil, M. Cernik, D.D. Dionysiou, Chemistry of persulfates in water and wastewater treatment: a review, *Chem. Eng. J.* 330 (2017) 44–62.
- [8] B.C. Hodges, E.L. Cates, J.-H. Kim, Challenges and prospects of advanced oxidation water treatment processes using catalytic nanomaterials, *Nat. Nanotechnol.* 13 (2018) 642–650.

[9] M. Gagol, A. Przyjazny, G. Boczkaj, Wastewater treatment by means of advanced oxidation processes based on cavitation - a review, *Chem. Eng. J.* 338 (2018) 599–627.

[10] Y. Bu, H. Li, W. Yu, Y. Pan, L. Li, Y. Wang, L. Pu, J. Ding, G. Gao, B. Pan, Peroxydisulfate activation and singlet oxygen generation by oxygen vacancy for degradation of contaminants, *Environ. Sci. Technol.* 55 (2021) 2110–2120.

[11] R. Su, N. Li, Z. Liu, X. Song, W. Liu, B. Gao, W. Zhou, Q. Yue, Q. Li, Revealing the generation of high-valent cobalt species and chlorine dioxide in the Co_3O_4 -activated chloride process: insight into the proton enhancement effect, *Environ. Sci. Technol.* 57 (2023) 1882–1893.

[12] Y. Wei, J. Miao, J. Ge, J. Lang, C. Yu, L. Zhang, P.J.J. Alvarez, M. Long, Ultrahigh peroxymonosulfate utilization efficiency over CuO nanosheets via heterogeneous $\text{Cu}(\text{III})$ formation and preferential electron transfer during degradation of phenols, *Environ. Sci. Technol.* 56 (2022) 8984–8992.

[13] Y. Gao, Y. Zhou, S.-Y. Pang, J. Jiang, Y.-M. Shen, Y. Song, J.-B. Duan, Q. Guo, Enhanced peroxymonosulfate activation via complexed $\text{Mn}(\text{II})$: a novel non-radical oxidation mechanism involving manganese intermediates, *Water Res.* 193 (2021), 116856.

[14] Z. Wang, W. Qiu, S.-Y. Pang, Q. Guo, C. Guan, J. Jiang, Aqueous iron(IV)-Oxo complex: an emerging powerful reactive oxidant formed by iron(ii)-based advanced oxidation processes for oxidative water treatment, *Environ. Sci. Technol.* 56 (2022) 1492–1509.

[15] R. Kumar, B. Pandey, A. Sen, M. Ansari, S. Sharma, G. Rajaraman, Role of oxidation state, ferryl-oxygen, and ligand architecture on the reactivity of popular high-valent Fe-IV=O species: a theoretical perspective, *Coord. Chem. Rev.* 419 (2020), 213397.

[16] Y. Zong, Y. Shao, Y. Zeng, B. Shao, L. Xu, Z. Zhao, W. Liu, D. Wu, Enhanced oxidation of organic contaminants by iron(II)-activated peroxide: the significance of high-valent iron-oxo species, *Environ. Sci. Technol.* 55 (2021) 7634–7642.

[17] Z. Wang, W. Qiu, S. Pang, Y. Gao, Y. Zhou, Y. Cao, J. Jiang, Relative contribution of ferryl ion species ($\text{Fe}(\text{IV})$) and sulfate radical formed in nanoscale zero valent iron activated peroxydisulfate and peroxymonosulfate processes, *Water Res.* 172 (2020), 115504.

[18] Y. He, Z. Wang, H. Wang, E. Almatrafi, H. Qin, D. Huang, Y. Zhu, C. Zhou, Q. Tian, P. Xu, G. Zeng, Confinement of ZIF-derived copper-cobalt-zinc oxides in carbon framework for degradation of organic pollutants, *J. Hazard. Mater.* 440 (2022), 129811.

[19] C. Zhu, S. Zhao, Z. Fan, H. Wu, F. Liu, Z. Chen, A. Li, Confinement of CoP nanoparticles in nitrogen-doped yolk-shell porous carbon polyhedron for ultrafast catalytic oxidation, *Adv. Funct. Mater.* 30 (2020) 2003947.

[20] M. Zhang, C. Xiao, X. Yan, S. Chen, C. Wang, R. Luo, J. Qi, X. Sun, L. Wang, J. Li, Efficient removal of organic pollutants by metal-organic framework derived Co/C yolk-shell nanoreactors: size-exclusion and confinement effect, *Environ. Sci. Technol.* 54 (2020) 10289–10300.

[21] L. Lyu, L. Zhang, Q. Wang, Y. Nie, C. Hu, Enhanced fenton catalytic efficiency of gamma-Cu-Al203 by sigma-Cu2+-ligand complexes from aromatic pollutant degradation, *Environ. Sci. Technol.* 49 (2015) 8639–8647.

[22] M. Liu, L. Wang, K. Zhao, S. Shi, Q. Shao, L. Zhang, X. Sun, Y. Zhao, J. Zhang, Atomically dispersed metal catalysts for the oxygen reduction reaction: synthesis, characterization, reaction mechanisms and electrochemical energy applications, *Energy Environ. Sci.* 12 (2019) 2890–2923.

[23] L.-S. Zhang, X.-H. Jiang, Z.-A. Zhong, L. Tian, Q. Sun, Y.-T. Cui, X. Lu, J.-P. Zou, S.-L. Luo, Carbon nitride supported high-loading Fe single-atom catalyst for activating of peroxymonosulfate to generate O-1(2) with 100% selectivity, *Angew. Chem. -Int. Ed.* 60 (2021) 21751–21755.

[24] Z. Zhao, W. Zhou, D. Lin, L. Zhu, B. Xing, Z. Liu, Construction of dual active sites on diatomic metal (FeCo-N/C-x) catalysts for enhanced Fenton-like catalysis, *Appl. Catal. B: Environ.* 309 (2022), 121256.

[25] Z. Wang, E. Almatrafi, H. Wang, H. Qin, W. Wang, L. Du, S. Chen, G. Zeng, P. Xu, Cobalt single atoms anchored on oxygen-doped tubular carbon nitride for efficient peroxymonosulfate activation: simultaneous coordination structure and morphology modulation, *Angew. Chem. -Int. Ed.* 61 (2022), e202202338.

[26] S. Bhunia, A. Rana, S.G. Dey, A. Ivancich, A. Dey, A designed second-sphere hydrogen-bond interaction that critically influences the O-O bond activation for heterolytic cleavage in ferric iron-porphyrin complexes, *Chem. Sci.* 11 (2020) 2681–2695.

[27] Y. Zong, H. Zhang, X. Zhang, W. Liu, L. Xu, D. Wu, High-valent cobalt-oxo species triggers hydroxyl radical for collaborative environmental decontamination, *Appl. Catal. B: Environ.* 300 (2022), 120722.

[28] J. Jiang, Z. Zhao, J. Gao, T. Li, M. Li, D. Zhou, S. Dong, Nitrogen vacancy-modulated peroxymonosulfate nonradical activation for organic contaminant removal via high-valent cobalt-oxo species, *Environ. Sci. Technol.* 56 (2022) 5611–5619.

[29] Y. He, Z. Yin, Z. Wang, H. Wang, W. Xiong, B. Song, H. Qin, P. Xu, G. Zeng, Recent progress on mixed transition metal nanomaterials based on metal-organic frameworks for energy-related applications, *J. Mater. Chem. A* 10 (2022) 9788–9820.

[30] Y. He, Z. Yin, Z. Wang, H. Wang, W. Xiong, B. Song, H. Qin, P. Xu, G. Zeng, Metal-organic frameworks as a good platform for the fabrication of multi-metal nanomaterials: design strategies, electrocatalytic applications and prospective, *Adv. Colloid Interface Sci.* 304 (2022), 102668.

[31] Y. He, Z. Wang, H. Wang, Z. Wang, G. Zeng, P. Xu, D. Huang, M. Chen, B. Song, H. Qin, Metal-organic framework-derived nanomaterials in environment related fields: fundamentals, properties and applications, *Coord. Chem. Rev.* 429 (2020), 213618.

[32] Z. Wang, P. Xu, H. Wang, E. Almatrafi, C. Zhou, Y. He, H. Yang, S. Chen, W. Tang, Z. Zeng, G. Zeng, Environmentally persistent free radicals in bismuth-based metal-organic layers derivatives: photodegradation of pollutants and mechanism unravelling, *Chem. Eng. J.* 430 (2022), 133026.

[33] L.-M. Cao, D. Lu, D.-C. Zhong, T.-B. Lu, Prussian blue analogues and their derived nanomaterials for electrocatalytic water splitting, *Coord. Chem. Rev.* 407 (2020), 213156.

[34] C. Chen, D. Xiong, M. Gu, C. Lu, F.-Y. Yi, X. Ma, MOF-Derived bimetallic CoFe-PBA composites as highly selective and sensitive electrochemical sensors for hydrogen peroxide and nonenzymatic glucose in human serum, *ACS Appl. Mater. Interfaces* 12 (2020) 35365–35374.

[35] V. Ganesan, J. Son, J. Kim, $\text{CoP}_2/\text{Fe-CoP}_2$ yolk-shell nanoboxes as efficient electrocatalysts for the oxygen evolution reaction, *Nanoscale* 13 (2021) 4569–4575.

[36] S. Ma, D. Yang, Y. Guan, Y. Yang, Y. Zhu, Y. Zhang, J. Wu, L. Sheng, L. Liu, T. Yao, Maximally exploiting active sites on Yolk@shell nanoreactor: nearly 100% PMS activation efficiency and outstanding performance over full pH range in Fenton-like reaction, *Appl. Catal. B: Environ.* 316 (2022), 121594.

[37] H. Li, S. Di, P. Niu, S. Wang, J. Wang, L. Li, A durable half-metallic diatomic catalyst for efficient oxygen reduction, *Energy Environ. Sci.* 15 (2022) 1601–1610.

[38] C. Zhang, C. Lai, G. Zeng, D. Huang, C. Yang, Y. Wang, Y. Zhou, M. Cheng, Efficacy of carbonaceous nanocomposites for sorbing ionizable antibiotic sulfamethazine from aqueous solution, *Water Res.* 95 (2016) 103–112.

[39] S. Zhang, H. Gao, X. Xu, R. Cao, H. Yang, X. Xu, J. Li, MOF-derived CoN/N-C@SiO_2 yolk-shell nanoreactor with dual active sites for highly efficient catalytic advanced oxidation processes, *Chem. Eng. J.* 381 (2020), 122670.

[40] M. Zhang, C. Wang, C. Liu, R. Luo, J. Li, X. Sun, J. Shen, W. Han, L. Wang, Metal-organic framework derived $\text{Co}_3\text{O}_4/\text{C@SiO}_2$ yolk-shell nanoreactors with enhanced catalytic performance, *J. Mater. Chem. A* 6 (2018) 11226–11235.

[41] P. Duan, Y. Qi, S. Feng, X. Peng, W. Wang, Y. Yue, Y. Shang, Y. Li, B. Gao, X. Xu, Enhanced degradation of clothianidin in peroxymonosulfate/catalyst system via core-shell FeMn@N-C and phosphate surrounding, *Appl. Catal. B: Environ.* 267 (2020), 118717.

[42] J. Miao, W. Geng, P.J.J. Alvarez, M. Long, 2D N-Doped porous carbon derived from polydopamine-coated graphitic carbon nitride for efficient nonradical activation of peroxymonosulfate, *Environ. Sci. Technol.* 54 (2020) 8473–8481.

[43] S. Liu, Z. Zhang, F. Huang, Y. Liu, L. Feng, J. Jiang, L. Zhang, F. Qi, C. Liu, Carbonized polyaniline activated peroxymonosulfate (PMS) for phenol degradation: role of PMS adsorption and singlet oxygen generation, *Appl. Catal. B: Environ.* 286 (2021), 119921.

[44] X. Liu, Y. Liu, H. Qin, Z. Ye, X. Wei, W. Miao, D. Yang, S. Mao, Selective removal of phenolic compounds by peroxydisulfate activation: inherent role of hydrophobicity and interface ROS, *Environ. Sci. Technol.* 56 (2022) 2665–2676.

[45] Y. Gao, Z. Chen, Y. Zhu, T. Li, C. Hu, New insights into the generation of singlet oxygen in the metal-free peroxymonosulfate activation process: important role of electron-deficient carbon atoms, *Environ. Sci. Technol.* 54 (2020) 1232–1241.

[46] X. Peng, J. Wu, Z. Zhao, X. Wang, H. Dai, L. Xu, G. Xu, Y. Jian, F. Hu, Activation of peroxymonosulfate by single-atom $\text{Fe-g-C}_3\text{N}_4$ catalysts for high efficiency degradation of tetracycline via nonradical pathways: Role of high-valent iron-oxo species and Fe-Nx sites, *Chem. Eng. J.* 427 (2022), 130803.

[47] Y. Gao, Y. Zhou, S.-Y. Pang, J. Jiang, Z. Yang, Y. Shen, Z. Wang, P.-X. Wang, L.-H. Wang, New insights into the combination of permanganate and bisulfite as a novel advanced oxidation process: importance of high valent manganese-oxo species and sulfate radical, *Environ. Sci. Technol.* 53 (2019) 3689–3696.

[48] N. Jiang, H. Xu, L. Wang, J. Jiang, T. Zhang, Nonradical oxidation of pollutants with single-atom- Fe(III) -activated persulfate: Fe(V) being the possible intermediate oxidant, *Environ. Sci. Technol.* 54 (2020) 14057–14065.

[49] C. Ying, B. Lanson, C. Wang, X. Wang, H. Yin, Y. Yan, W. Tan, F. Liu, X. Feng, Highly enhanced oxidation of arsenite at the surface of birnessite in the presence of pyrophosphate and the underlying reaction mechanisms, *Water Res.* 187 (2020), 116420.

[50] C. Zhou, Y. Liang, W. Xia, E. Almatrafi, B. Song, Z. Wang, Y. Zeng, Y. Yang, Y. Shang, C. Wang, G. Zeng, Single atom Mn anchored on N-doped porous carbon derived from spirulina for catalyzed peroxymonosulfate to degradation of emerging organic pollutants, *J. Hazard. Mater.* 441 (2023), 129871.

[51] X. Mi, H. Zhong, H. Zhang, S. Xu, Y. Li, H. Wang, S. Zhan, J.C. Crittenden, Facilitating redox cycles of copper species by pollutants in peroxymonosulfate activation, *Environ. Sci. Technol.* 56 (2022) 2637–2646.

[52] Y. Yao, C. Wang, X. Yan, H. Zhang, C. Xiao, J. Qi, Z. Zhu, Y. Zhou, X. Sun, X. Duan, J. Li, Rational regulation of Co-N-C coordination for high-efficiency generation of O-1(2) toward nearly 100% selective degradation of organic pollutants, *Environ. Sci. Technol.* 56 (2022) 8833–8843.

[53] N. Li, R. Li, X. Duan, B. Yan, W. Liu, Z. Cheng, G. Chen, La Hou, S. Wang, Correlation of active sites to generated reactive species and degradation routes of organics in peroxymonosulfate activation by co-loaded carbon, *Environ. Sci. Technol.* 55 (2021) 16163–16174.

[54] J. He, Y. Wan, W. Zhou, ZIF-8 derived Fe-N coordination moieties anchored carbon nanocubes for efficient peroxymonosulfate activation via non-radical pathways: role of FeNx sites, *J. Hazard. Mater.* 405 (2021), 124199.

[55] T.N. Das, Reactivity and role of SO_5 center dot- radical in aqueous medium chain oxidation of sulfite to sulfate and atmospheric sulfuric acid generation, *J. Phys. Chem. A* 105 (2001) 9142–9155.

[56] A.N. Yermakov, G.A. Poskrebshev, S.I. Stoliarov, Temperature dependence of the branching ratio of SO_5 radicals self-reaction in aqueous solution, *J. Phys. Chem.* 100 (1996) 3557–3560.

[57] D. Gao, Y. Lu, Y. Chen, M. Bao, N. Xu, Novel CoFe₂Px derived from CoFe₂O₄ for efficient peroxymonosulfate activation: Switching the reaction route and suppressing metal leaching, *Appl. Catal. B: Environ.* 309 (2022) 121234.

[58] R. Luo, M. Li, C. Wang, M. Zhang, M.A.N. Khan, X. Sun, J. Shen, W. Han, L. Wang, J. Li, Singlet oxygen-dominated non-radical oxidation process for efficient degradation of bisphenol A under high salinity condition, *Water Res.* 148 (2019) 416–424.

[59] L. Wang, J. Jiang, S.-Y. Pang, Y. Zhou, J. Li, S. Sun, Y. Gao, C. Jiang, Oxidation of bisphenol A by nonradical activation of peroxymonosulfate in the presence of amorphous manganese dioxide, *Chem. Eng. J.* 352 (2018) 1004–1013.

[60] Z.-H. Xie, C.-S. He, H.-Y. Zhou, L.-L. Li, Y. Liu, Y. Du, W. Liu, Y. Mu, B. Lai, Effects of molecular structure on organic contaminants' degradation efficiency and dominant ROS in the advanced oxidation process with multiple ROS, *Environ. Sci. Technol.* 56 (2022) 8784–8795.

[61] H. Li, C. Shan, B. Pan, Fe(III)-Doped g-C₃N₄ mediated peroxymonosulfate activation for selective degradation of phenolic compounds via high-valent iron-oxo species, *Environ. Sci. Technol.* 52 (2018) 2197–2205.

[62] P. Hu, H. Su, Z. Chen, C. Yu, Q. Li, B. Zhou, P.J.J. Alvarez, M. Long, Selective degradation of organic pollutants using an efficient metal-free catalyst derived from carbonized polypyrrole via peroxymonosulfate activation, *Environ. Sci. Technol.* 51 (2017) 11288–11296.

[63] T. Ye, Z. Wei, R. Spinney, D.D. Dionysiou, S. Luo, L. Chai, Z. Yang, R. Xiao, Quantitative structure-activity relationship for the apparent rate constants of aromatic contaminants oxidized by ferrate (VI), *Chem. Eng. J.* 317 (2017) 258–266.